UNDERSEA ROBOTS

Miniature deep-sea morphable robot with multimodal locomotion

Fei Pan[1,2]†, Jiaqi Liu[1]†, Zonghao Zuo[1]†, Xia He[1]†, Zhuyin Shao[1], Junyu Chen[1], Haoxuan Wang[1], Qiyi Zhang[1], Feiyang Yuan[1], Bohan Chen[1], Tongtong Jin[1], Liwen He[1], Yun Wang[1], Kangle Zhang[3], Xilun Ding[1]*, Tiefeng Li[4,5], Li Wen[1]*

Research on miniature deep-sea robots is an emerging field focused on the development of deployable, compact devices capable of interacting with the unique environments and organisms of the deep ocean. In this study, we present a design strategy for a centimeter-scale deep-sea soft actuator, weighing 16 grams, that incorporates bistable chiral metamaterials and tube-sealed shape memory alloys. According to our design, the increased modulus induced by the hydrostatic pressure was used to achieve a higher snapping velocity of the bistable chiral unit, thus lifting the actuator's performance. We showed that the actuator can produce undistorted cyclic motions at various depths in the deep sea. Subsequently, we developed an untethered miniature deep-sea robot that is capable of multimodal locomotion by repurposing its legs and fins. To validate the robot's performance, this miniature robot was deployed from deep-sea crewed submersibles, performing swimming, gliding, morphing, and crawling in the Haima Cold Seep (1380-meter depth) and the Mariana Trench (10,600-meter depth); it was then retrieved by the submersible fully intact. The actuation module design enabled the robot to perform comparably in the Haima Cold Seep and laboratory aquarium conditions (atmospheric pressure). Additionally, we developed a wearable soft gripper based on the same metamaterial design strategy to facilitate safe deep-sea operations, ranging from soft-specimen collection to heavy-object manipulation (~3400-meter depth). This study offers design insights into creating next-generation miniature deep-sea actuators and robots, paving the way for future exploration and interaction with deep-sea ecosystems.

INTRODUCTION

The deep sea remains one of the least-explored regions of our planet, prompting researchers to seek careful and nondestructive methods for studying this delicate ecosystem (*1*). Traditional deep-sea vehicles, often bulky and cumbersome, can create notable turbulence and damage fragile habitats when operating in close proximity. In contrast, a lightweight, deployable, untethered miniature robot (centimeter scale) offers opportunities for exploring these ecosystems and conducting in situ measurements with minimal disturbance. Deep-sea organisms that exhibit multimodal locomotion provide valuable inspiration for the development of robots with versatile capabilities. For instance, batfish use finely tuned movements of their fins, functioning as limbs and flippers, to swim or walk in the deep sea (*2*). Similarly, frogfish have pectoral and pediculate fins for fin-assisted walking on benthic substrates, maneuvering through rocky terrain, and navigating between whale bones (*3*). These natural adaptations underscore the potential for biomimetic multimodal designs in the robotic exploration of deep-sea environments.

Developing a deep-sea multimodal miniature robotic system presents two major challenges. First, the miniaturization of the actuation system for an untethered deep-sea robot poses a notable challenge. Traditional rigid actuation components, such as hydraulic cylinders and motors, are both bulky and heavy. Although advancements have been made in miniaturizing waterproof and pressure-tolerant motors (*4*), they remain unsuitable for integration into centimeter-scale robots designed for deep-sea applications, particularly those requiring multiple actuators for complex locomotion. Hydraulic soft actuators, although promising, require bulky pumps and pressure-regulating components, complicating their use in miniature designs (*5*–*11*). Although dielectric elastomer actuators (DEAs) have been incorporated into deep-sea soft robotic fish, their performance—specifically, the amplitude and maximum velocity of cyclic motion—diminishes under the high-pressure deep-sea conditions (*12*). Thus, achieving the desired deformation and superior performance through a compact actuation system in deep-sea environments remains a considerable challenge.

Second, recent studies have introduced machines constructed from soft materials that can withstand the high pressures of deep-sea environments. For instance, a snailfish-inspired robot is capable of flapping its fins to swim (*12*), a fluidic-actuated soft gripper can bend or twist to grasp deep-sea corals (*5*–*10*), and a jamming gripper can enclose deep-sea objects for capture (*11*). However, these robots are limited to simple, single-mode locomotion and lack the ability to morph or engage in multiple locomotor modes necessary for adapting to the dynamic and extreme conditions of the deep sea. Consequently, bioinspired multimodal locomotion in miniature deep-sea robots remains less explored.

In this study, we integrated specialized swimming and benthic locomotion features to develop a morphable multimodal robot for deep-sea exploration, using a previously undescribed type of soft actuator. Miniature soft actuation modules based on mechanical metamaterials provide a broad design space for bioinspired multimodal locomotion (*13*–*25*). These modules are ideal candidates for enabling large-amplitude, high-force output and can be easily fabricated at various scales. Our soft actuator (centimeter scale, weighing

---

[1] School of Mechanical Engineering and Automation, Beihang University, Beijing, China. [2] School of Aeronautic Science and Engineering, Beihang University, Beijing, China. [3] Institute of Deep-sea Science and Engineering, Chinese Academy of Sciences, Sanya, China. [4] Center for X-Mechanics, Zhejiang University, Hangzhou, China. [5] Institute of Fundamental and Transdisciplinary Research, Zhejiang University, Hangzhou, China.
†These authors contributed equally to this work.
*Corresponding author. Email: liwen@buaa.edu.cn (L.W.); xlding@buaa.edu.cn (X.D.)

16 g) can tolerate high pressure because of its incompressible components (*26*, *27*). This actuator enables the robot to produce superior cyclic motions in deep-sea conditions that are comparable to its performance in atmospheric pressure conditions in a laboratory aquarium. Furthermore, the mechanical metamaterial–based soft actuators are capable of enhancing performance with increasing hydrostatic pressure by leveraging the snapping phenomenon of flexible structures. The self-contained miniature robot, with a total weight of 2.7 kg in air, is designed to reversibly switch between multiple modes of locomotion and can be deployed and retrieved by a crewed deep-sea submersible. We demonstrate that this robot effectively swims, glides, and crawls in the Haima Cold Seep (depth, ~1380 m) and the Mariana Trench (depth, ~10,600 m). Additionally, we illustrate that a soft gripper based on our proposed metamaterial structure can be integrated with a rigid gripper to delicately grasp various deep-sea organisms.

RESULTS

Miniature robots exhibiting multimodal locomotion in the deep sea

Soft actuation modules based on mechanical metamaterials offer a versatile design framework for enabling multimodal locomotion of deep-sea robots. We have developed a chiral bistable unit, precompressed from a cross-shaped soft precursor, capable of achieving either a clockwise (left-handed) or counterclockwise (right-handed) twisted state. The chiral unit's typical bistable feature (for example, snap-through motion and morphing) was used for a miniaturized robot design. The compression-torsion coupling feature of the chiral unit was also used in the design of a deep-sea soft gripper (Fig. 1A and movie S1).

The miniaturized robot was preprogrammed and deployed from a crewed submersible at depths of 1385 m in the Haima Cold Seep and 10,600 m in the Mariana Trench, executing untethered multimodal locomotion, including swimming and gliding (Fig. 1, B, D, and F, and Movie 1) as well as crawling along the seabed (Fig. 1, C, E, and G). Throughout these operations, the robot dynamically morphed to facilitate different modes of locomotion by mechanically programming its fins and legs. The locomotion was primarily driven by large-amplitude movements of the actuation modules, resulting in an average swimming speed of 33.7 mm/s (0.134 body length/s) and an average crawling speed of 21.5 mm/s (0.086 body length/s) in the Haima Cold Seep (Fig. 1, D and E) and a swimming and gliding speed of 33.3 mm/s (0.133 body length/s) in the Mariana Trench (Fig. 1F). After these missions, the deep-sea submersible retrieved the robot using its robotic arm (Fig. 1G).

Additionally, the deep-sea soft gripper was designed to be easily "worn" on the existing rigid gripper of the submersible (Fig. 1A). We demonstrated that the gripper can perform practical deep-sea tasks, such as repositioning a heavy lander (Fig. 1H), opening a sampling box (Fig. 1K), collecting biological samples (for example, sea cucumbers and starfish) at depths exceeding 3500 m, and subsequently placing the samples in a collection box (Fig. 1, I and J).

Deep-sea soft actuation using chiral metamaterials and tube-sealed SMA

High hydrostatic pressure and low temperatures pose notable challenges for small-scale actuators in deep-sea environments. As previously reported, the elevated hydrostatic pressure conditions in the deep sea increase the Young's modulus of soft materials (*28*). This increase in stiffness negatively influences the performance of soft actuators, including DEAs (*4*), piezoelectric actuators (*29*), and magnetic actuators (*30*), because their constituent materials become stiffer under high pressure. In this work, we leveraged the rapid snap-through motion of a bistable elastic structure to design a type of deep-sea actuator that can overturn the shortness imposed by the increased modulus because of hydrostatic pressure.

To realize the deep-sea robot's cycling swing motion, we designed a cavity-free, bistable chiral unit with left-handed or right-handed states. When switching between the two stable states, this unit can generate a torsional snapping motion (*31*, *32*). More specifically, the chiral unit was precompressed from a cross-shaped soft structure precursor to exhibit clockwise (left-handed) and counterclockwise (right-handed) stable states, with a twisted angle of $\pm\theta_{\text{stable}}$, respectively (Fig. 2A). A torsional load can elastically and reversibly switch the left-handed and right-handed states of the unit (Fig. 2D). Under a torsional angle-controlled quasistatic loading from $-\theta_{\text{stable}}$ to $+\theta_{\text{stable}}$, the reaction torque of the unit presents a typical N-shape profile (Fig. 2D). At the critical point when the torque changes from positive to negative, the structure can spontaneously fast snap to the other state upon removing the loading boundary condition (Fig. 2B). Also, under a torque-controlled loading condition, the snap-through behavior occurs at the peak of torque (T_{peak}) when entering the negative stiffness regime. In theory (*33*), the snapping velocity ω of the bistable structure is proportional to the square root of the ratio of Young's modulus E to material density ρ (Fig. 2A). Therefore, the increased modulus induced by the high hydrostatic pressure and low temperature can be used to achieve a higher snapping velocity that benefits the soft actuator's performance.

From Fig. 2A, the bistable soft actuator could achieve higher snapping velocity through increased modulus induced by hydrostatic pressure. Increasing the modulus of the soft materials (because of the hydrostatic pressure) allows the structure to store more elastic energy, which can then be released as kinetic energy during the snapping process (Fig. 2D). This results in higher velocity (Fig. 2B) and increased output power (fig. S1G). Meanwhile, without an external payload, the kinetic energy can make the unit's torsional angle reach beyond the stable state angle $+\theta_{\text{stable}}$, showing a larger swing amplitude that can be increased by increasing the modulus (Fig. 2B). Additionally, the released kinetic energy can generate output torque to overcome external payload. The output torque is proportional to Young's modulus, which is well demonstrated by the theory, finite element analysis (FEA) simulation, and experimental results (Fig. 2C).

We estimated a 15.1% increase in the soft materials modulus at 120 MPa, equal to the hydrostatic pressure of a 12,000-m depth (*30*). The angle-velocity profiles of the spontaneous snapping process obtained by FEA are shown in Fig. 2B. Compared with the one with a reference modulus of E_0, the structure with the modulus of 1.15 E_0 enables an 8.50% higher maximum snapping velocity and a 1.68% increase in torsional amplitude. The applied torque-angle profile of the angle-controlled quasistatic loading is shown in Fig. 2D. The applied torque shows a 15.3% increase with a 15.1% increase in the soft material's modulus, indicating that a 15.3% additional torque is needed to trigger the snapping process.

To facilitate this principle in the design of a deep-sea actuator, we used shape memory alloy (SMA) springs to trigger the snapping. Here, we used a tube sealing method to ensure that the SMA spring

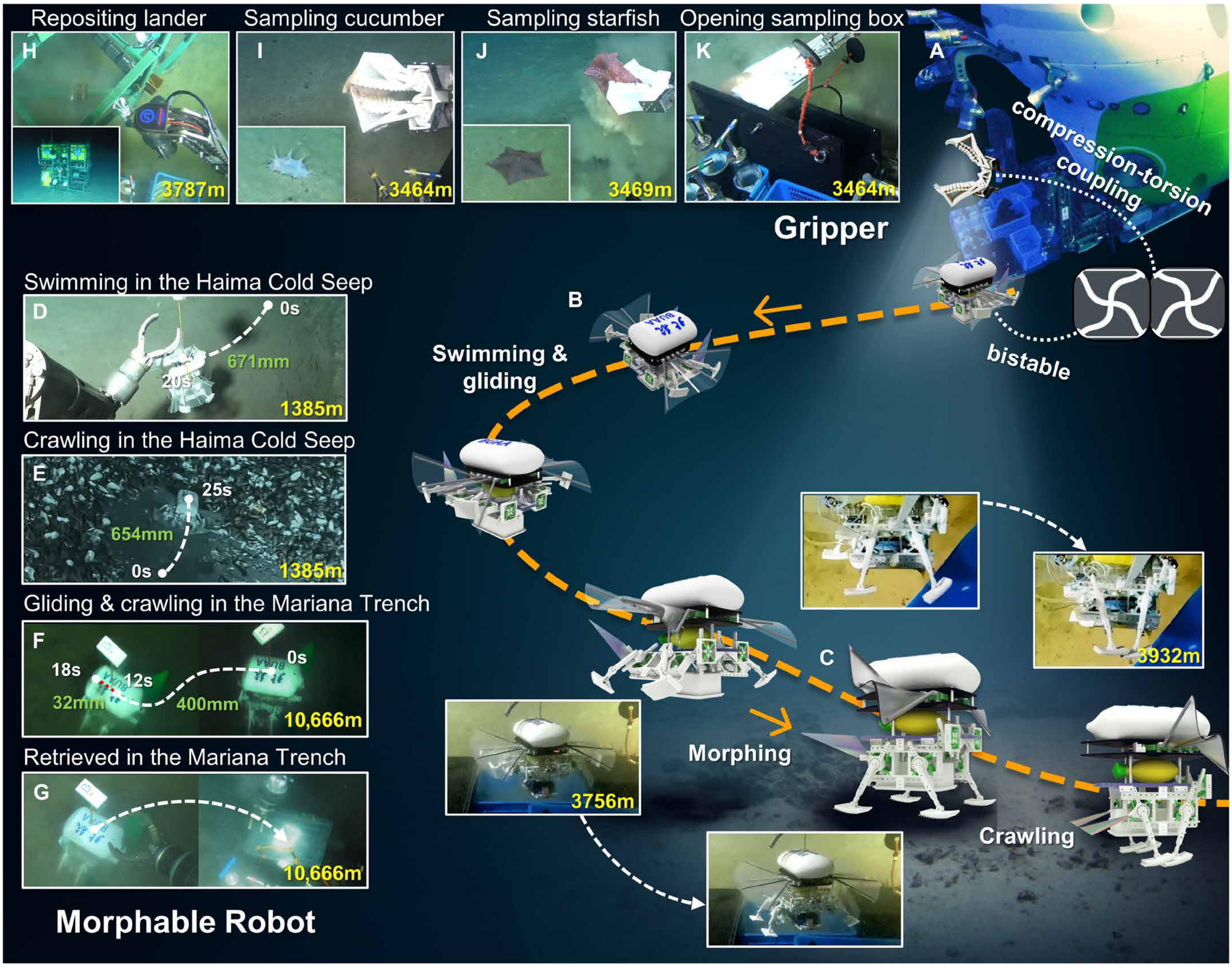

Fig. 1. Mission profile of the deep-sea multimodal soft robot, showing its capabilities to swim, glide, crawl, and grasp in deep-sea environments. (**A**) The small-scale robot was deployed by the Fendouzhe crewed submersible at a depth of 10,666 m, demonstrating untethered, morphable, and multimodal locomotion. (**B**) The robot swimming and gliding with fins open. (**C**) The robot crawling on the seabed with fins closed. (**D**) The robot swam 671 mm in 20 s in the Haima Cold Seep. (**E**) The robot crawled 654 mm in 25 s in the Haima Cold Seep. (**F**) The robot swam and glided 400 mm in 12 s in the Mariana Trench. The small robot crawled 32 mm in 6 s in the Mariana Trench. (**G**) The robot being retrieved by the rigid robotic arm of the Fendouzhe submersible. (**H**) The soft gripper mounted on the rigid arm of the Deep Sea Warrior, repositioning a heavy deep-sea lander (Canghai) at a depth of 3787 m in the South China Sea. (**I**) The soft gripper collecting a sea cucumber at 3464 m in the South China Sea. (**J**) The soft gripper collecting a deep-sea starfish at 3469 m in the South China Sea. (**K**) The soft gripper manipulating the collection box for biological samples. Further details on the robot's multimodal locomotion are available in movies S11 to S13, and additional information on deep-sea sampling can be found in movie S14.

functioned properly and resisted the high pressure in the deep-sea environment. More specifically, we sealed the SMA spring in a silicone hose, connected it to the power and control system, wrapped it in a soft shell, and filled the void with silicone oil to isolate it from the seawater (fig. S3). The performance of the tube-sealed SMA spring is shown in table S1.

Next, we implemented a deep-sea chiral actuation module that combines the SMA spring and the chiral unit (Fig. 2E). Specifically, we integrated two antagonistic SMA springs with a pair of chiral units to produce periodic oscillations. The SMA spring on each side of the chiral unit shortens cyclically to realize an oscillation motion. Compared with achiral units, the chiral actuation module can increase the rotational amplitude (with an average and maximum increase of 71.6 and 99.7%, respectively) in the frequency range of 0.1 to 0.6 Hz (Fig. 2, F and G). The deep-sea chiral actuation module can actuate with a torsional speed of 175°/s and a maximum torque of 0.2 N·m, and it has a life span of 1590 cycles.

We also tested the deep-sea chiral actuation module at different pressures and temperatures to mimic deep-sea conditions and validate the actuator's feasibility. Our results show that the rotational amplitude of the module under natural deep-sea conditions (4°C, 40 MPa) was larger (with maximum and average increases of 26.6 and 21.7%, respectively) than that under normal temperature and pressure (22°C, 100 kPa), as shown in Fig. 2 (I and J). The chiral units

Movie 1. Overview of the deep-sea miniature multimodal robot.

could generate 26.2 ± 2.7° (error values are ±1 SD) of rotational amplitude and a 121.9 ± 16.3°/s snapping velocity in the lab water tank; in contrast, the robot generated 32.3 ± 3.8° of rotational amplitude and 142.9 ± 40.5°/s snapping velocity in a deep-sea environment at a depth of 3932 m (movie S11). These results ensure that the robot's soft actuation is performant in the deep, real-world aquatic environment.

Performance of miniature robot's multimodal locomotion in the deep sea

We designed an untethered, morphable robot with swimming, gliding, and crawling locomotion modes. The robot was designed with foldable pectoral fins for gliding (with fins open), two symmetrical tail fins for swimming, and a set of legs for crawling (fig. S6A). It can reversibly switch between any of these modes of locomotion. By exploiting the two stable states of the chiral unit with an angle difference of 90°, a morphable module (Fig. 3A) was designed to realize the ability to morph between the swimming and crawling modes. The tail fin and the two legs on the same side share a metamaterial actuation module. Using the compression-bending coupling of the chiral unit array (Fig. 3A, fig. S1, and movie S2), we also designed a folding module that retracted the gliding fins by contracting a set of SMA springs. A propulsion module was designed using the fast snapping switching of the two stable states, which endows the swimming and crawling modes with periodic paddling locomotion. The robot was powered by an onboard lithium battery (2600 mA·hour) and controlled by an onboard microcontroller unit circuit (Fig. 3B and fig. S6F).

We tested the robot's locomotion in a laboratory aquarium measuring 1.0 m by 4.0 m by 8.0 m (movies S6 and S7), equipped with a camera positioned above to record the robot's movement. In swimming mode, the SMA springs actuate the chiral unit, allowing it to transition between two stable states and creating a paddling motion in the tail fins to generate forward thrust (Fig. 3C). The robot achieved a maximum swimming speed of 60.8 mm/s. By actuating the metamaterial actuation modules on either side of the robot, it can effectively control its swimming direction (Fig. 3, D and E). Additionally, the robot can generate complex motion trajectories through sequential actuation of the tail fin (Fig. 3F).

During gliding in the lab water tank, the extended pectoral fins enabled the robot to glide for considerable distances because of the upward hydrodynamic lift force acting on them. With the pectoral fins retracted, the robot glided 210 mm. When the pectoral fins were opened, it could glide 880 mm without tail fin actuation. With the pectoral fins open and the tail fin activated, the robot achieved a glide distance of 1430 mm. These results indicate that foldable pectoral fins enhance the robot's gliding capability, thereby conserving energy during locomotion and allowing for adjustments to the landing location (Fig. 3G and fig. S7G).

Furthermore, the rapid state-switching capability of the morphable module enables the robot to transition from swimming to crawling mode within 0.75 s upon landing (Fig. 3H), primarily relying on the SMA springs to adjust the chiral unit at the front of the robot. Meanwhile, the pectoral fins retract over a duration of 1.5 s. In crawling mode (Fig. 3I), the robot repurposes the same actuators from swimming to paddle its anisotropic feet, generating forward friction forces synchronized with the paddling motion of the tail fins (fig. S6D). Actuating the metamaterial actuation modules on both sides of the robot also allows for directional control during crawling (fig. S7H). The robot can achieve a maximum crawling speed of 31 mm/s (fig. S7I), and this speed can be further enhanced by increasing the actuation frequency and foot size (movie S8).

We also measured the propulsion force generated by the fins and legs when swimming and crawling. Under the same actuation

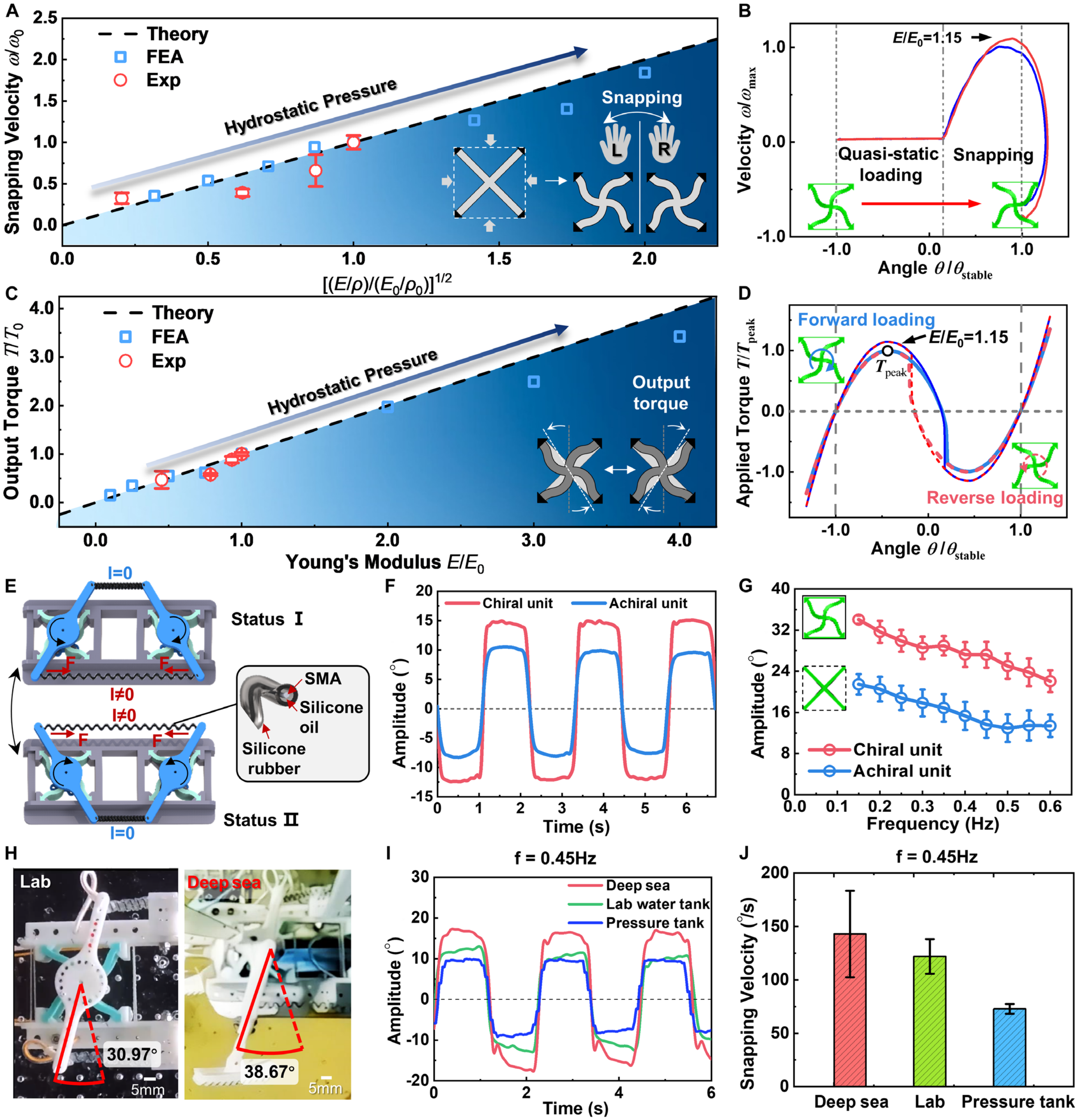

Fig. 2. The deep-sea chiral actuation module. (**A**) The relationship between the snapping velocity of the chiral actuation module and Young's modulus (*E*) and density (ρ) (*n* = 5; error bars indicate the SD). (**B**) Velocity of the chiral unit during the state-switching process. (**C**) The relationship between the output torque of the chiral actuation module and Young's modulus (*E*) (*n* = 5; error bars indicate the SD). (**D**) Applied torque on the chiral unit during state-switching under angle-controlled loading conditions. (**E**) Design schematic of the deep-sea chiral actuation module; the SMA coil is sealed with silicone oil within a silicone rubber tube. (**F**) Temporal variations in swing angles for chiral and achiral actuation modules. (**G**) Comparison of the rotational amplitudes for chiral and achiral actuation modules in a laboratory water tank (*n* = 10; error bars indicate the SD). Further details regarding the chiral and achiral comparison are available in movie S3. (**H**) Comparison of the rotational amplitudes of the chiral units in the lab and deep-sea environments (additional details about the pressure tank tests are available in movie S5). (**I** and **J**) Comparison of the rotational amplitudes of the chiral actuation modules in a pressure tank (hydrostatic pressure, 40 MPa; temperature, 30°C), laboratory water tank (hydrostatic pressure, 0 MPa; temperature: 22°C), and deep-sea environment (depth, 3789 m; corresponding hydrostatic pressure, 37.9 MPa; temperature, 4°C) under an actuation frequency of 0.45 Hz (*n* = 5; error bars indicate the SD).

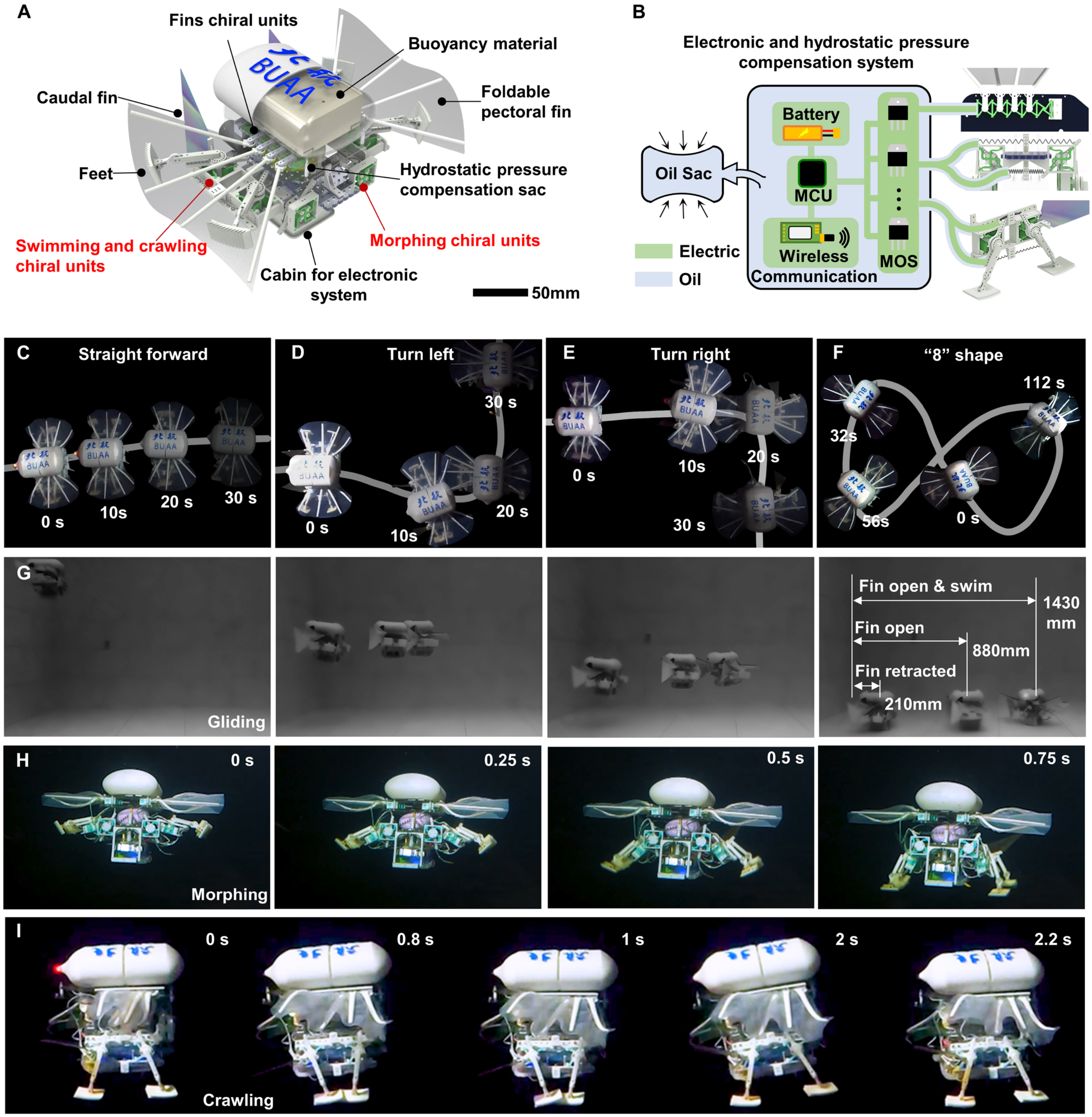

Fig. 3. Multimodal locomotion of the robot in the laboratory tank under atmospheric conditions. (**A**) Overall design of the robot. (**B**) Schematic of the robot's circuit and pressure compensation system. (**C**) The robot swimming in a straight line. (**D**) The robot making a left turn. (**E**) The robot making a right turn. (**F**) The robot following an "8"-shaped trajectory. (**G**) Gliding test results: landing distances for the robot in different configurations—210 mm with fins retracted, 880 mm with fins extended, and 1430 mm while swimming forward with fins extended. (**H**) Transition from the swimming state to the crawling state. (**I**) Critical frames of the robot's walking procedure. Additional details regarding the robot's multimodal locomotion in the laboratory water tank are available in movies S6 and S7.

parameters, the bearing-pin mechanism could generate a propulsion force of 0.120 ± 0.01 N. In contrast, the chiral unit could generate a propulsion force of 0.370 ± 0.01 N. Therefore, compared with the classic rigid mechanism, the chiral transmission enhanced the propulsion force by 208%. We also show that the propulsion force increased as the modulus of the soft materials increased with deeper depth and lower water temperature (fig. S7B). Then, we measured the crawling forces on smooth (acrylic board) and rough (100-grit sandpaper) surfaces in a lab aquarium. Our results show that the forward frictional force generated by the legs on the rough surface alone was 1.06 ± 0.02 N and that the force generated by both legs and fins was 1.38 ± 0.25 N. The flapping fins enhanced the crawling propulsion force on rough surfaces by 30.1% (fig. S7D).

The robot was deployed into the deep sea via a crewed submersible and tested at three distinct locations with varying depths: Haima Cold Seep (1384 m), Longxi Seamount (3756 m), and Mariana Trench (10,666 m) (Fig. 4A). The miniature robot was specifically tested at the Haima Cold Seep in the South China Sea at a depth of 1384 m using the Deep Sea Warrior crewed submersible (Fig. 4, B to F, and movie S12). Before the experiment, we adjusted the robot's weight on the mother ship to ensure that its density was slightly greater than that of seawater at the intended diving depth. To validate the design, the robot was positioned in front of the submersible within the workspace of its robotic arm, lifted from the front rack, and released ~2 m above the seafloor. During the test, the robot swam a distance of 671 mm in 20 s and crawled 654 mm in 25 s at Haima Cold Seep (movie S12). The results demonstrated that the deep-sea chiral actuation module facilitated comparable performance in both deep-sea and laboratory environments, with swimming velocities of 33.7 mm/s in the deep sea and 33.1 mm/s in the lab; swimming and gliding velocities of 72.1 mm/s in the deep sea and 56.9 mm/s in the lab; and crawling velocities of 21.5 mm/s in the deep sea and 27.7 mm/s in the lab.

The robot was subsequently deployed by the Fendouzhe crewed submersible at a depth of 10,666 m, where it swam and glided a distance of 400 mm in 12 s in the Mariana Trench. Additionally, the robot crawled 32 mm in 6 s at an actuation frequency of 0.45 Hz, although its swimming velocity experienced a slight decrease at this depth. Ultimately, the robot was retrieved using a rigid robotic arm (movie S13). To our knowledge, this marks one of the very limited reports on a freely moving miniaturized robot performing multimodal locomotion in the Mariana Trench.

Versatile deep-sea manipulation using a gripper designed with chiral metamaterials

We also developed a three-dimensionally (3D) printed soft gripper on the basis of the chiral design strategy, which can be worn on a rigid robotic gripper (Fig. 5A). The design principle leverages the compression-torsion effect inherent to chiral metamaterials. Our results demonstrate that the center of the chiral unit twists under unidirectional compression, converting linear motion into rotation through compression-torsion coupling (Fig. 5C and movie S1). This unit exhibits a prolonged plateau regime during compression, indicating stable performance under compressive force (Fig. 5B). Additionally, it displays unique mechanical properties compared with conventional materials, such as transverse shearing deformation when compressed (compression-shear coupling) (Fig. 5C). Consequently, the combination of compression-torsion and compression-shear coupling offers a wide design space for achieving complex deformations with simple, single–degree-of-freedom actuation.

The soft gripper consists of two symmetrical chiral units and a pair of grasping fingers. Each finger features an L-shaped outer support, an inner section embedded with microchiral structures to enhance grasping contact, and a claw-shaped tip for effective encapsulation. The soft gripper can be worn on a rigid gripper using Z-shaped connectors, with the rigid gripper providing linear actuation for the chiral units. The compression-torsion coupling effect of the chiral units enables the rotation of the two fingers, facilitating the gripping motion of the gripper (Fig. 5, D and E). This coupling effect also results in a long plateau region during the grasping process, whereby after the fingers close, the gripping force does not increase with additional linear loading at the base. This plateau region would enhance the protection of the grasped object.

To evaluate the grasping capability of the soft gripper, we conducted pull-off force tests using objects with various shapes (sphere, cylinder, and hexagonal prism) and sizes (40, 60, and 80 mm in diameter) (movie S9). The results indicate that the soft gripper achieved a maximum tangential gripping force of 28.3 N for spherical objects, 12.8 N for cylindrical objects, and 51.8 N for hexagonal objects (Fig. 5F). The claw-shaped tip also contributed to a maximum gripping force of 10 N (fig. S8). We designed microchiral structures for the contact surface that interfaces with the grasped object, which can rotate and conform to the object's surface under the applied gripping force (movie S10). We also compared the contact stress of the right-handed and left-handed microchiral structures. The results show that the right-handed microchiral structures displayed more uniform contact stress (fig. S9 and movie S10).

To demonstrate the adaptability of the robot's grasping ability in the deep sea, we assessed its performance in grasping both soft and rigid objects. We recorded the contact stress during the grasping motion (Fig. 5G) and calculated the deformation ratio on the basis of changes in the object radius. The results revealed that the gripper maintained low contact stress (<33 kPa) and a small range of deformation (0 to 14%) across a wide variety of objects, with Young's modulus values ranging from 10^4 to 10^9 Pa (Fig. 5H).

The metamaterial gripper was deployed by the Fendouzhe crewed submersible during a scientific expedition in the South China Sea, reaching a maximum depth of 3469 m (fig. S10A). After landing on the seafloor, we tested the gripper's capability to collect biological specimens by retrieving various deep-sea organisms, including a starfish, sea urchin, and sea cucumber (fig. S8, B and D, and movie S14). The biological collection box was a sealed container, specifically designed to maintain the environmental temperature at the depth where the organisms reside. We opened the box using the soft robotic gripper before grasping the organisms (fig. S10C), and it remained securely closed once the sampling task was completed (fig. S10D).

Real-world deep-sea submersible missions are often associated with diverse task requirements and limited operational time. The current gripper does not require an external power supply and can be worn on the existing rigid end effector system. Our results show that the proposed gripper can perform multiple tasks, including biological sampling, opening and closing containers, and repositioning a lander (fig. S10E). In addition, it is capable of completing delicate grasping motions in 2 s. Our deep-sea field tests also show that this gripper can perform a wider range of tasks compared with previous deep-sea gripper prototypes (table S2).

DISCUSSION

In this paper, we demonstrate the multimodal locomotion of a self-contained miniature robot in the deep sea, using a hydrostatic pressure-resistant integrated chiral soft actuator. The performance of this actuator is comparable under both laboratory and deep-sea conditions. We leveraged the instability-induced snapping motion of a bistable metamaterial structure, which is enhanced by the increased

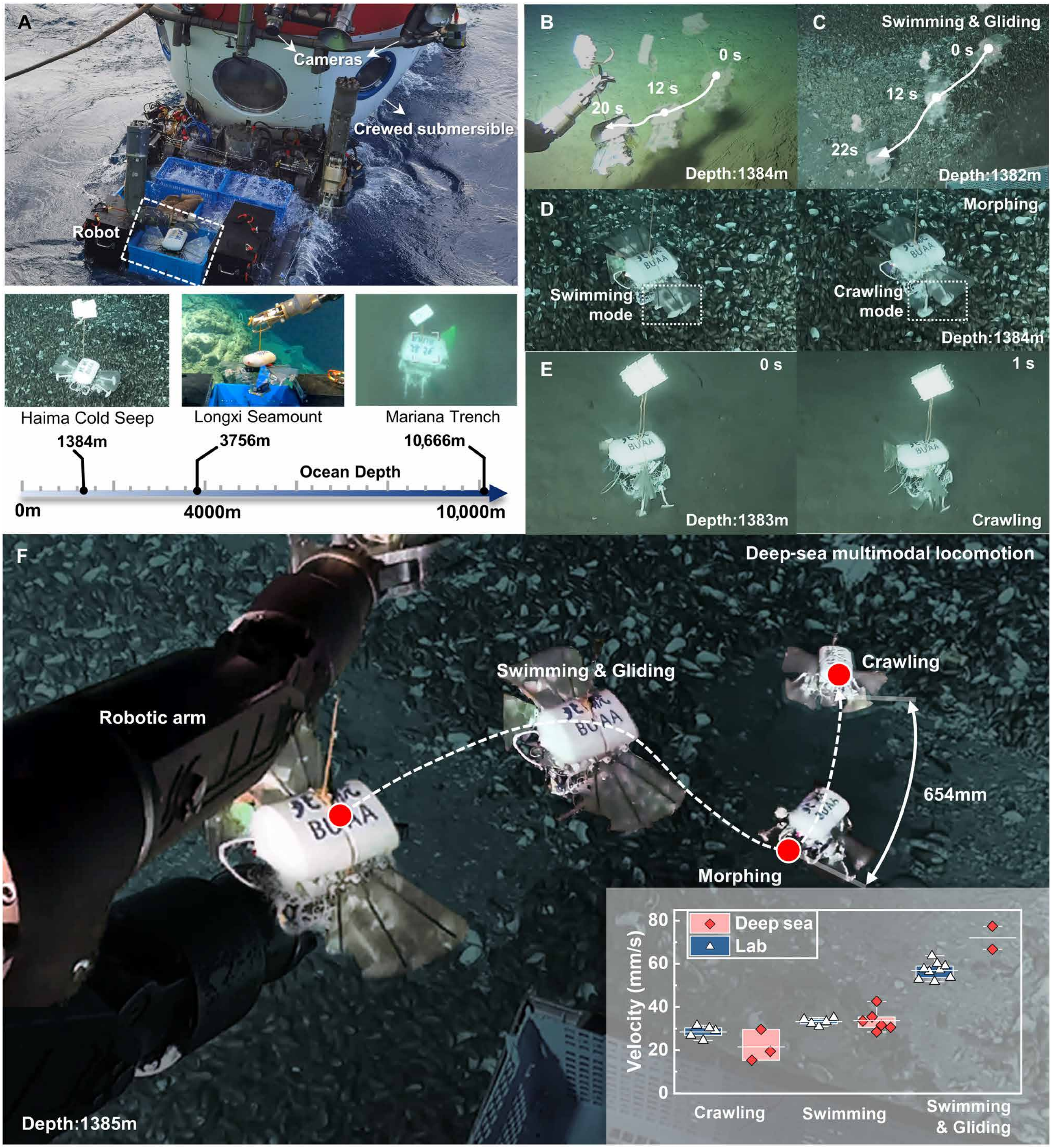

Fig. 4. Multimodal locomotion of the robot in the deep sea. (**A**) The robot being transported by the Deep Sea Warrior crewed submersible before diving. (**B** and **C**) Swimming and gliding tests conducted in the deep sea. (**D**) Transition between swimming and crawling modes. (**E**) Crawling of the robot. (**F**) Trajectories from experiments deploying the robot in the deep sea; the subpanel compares the robot's velocities between the laboratory water tank (crawling, $n = 5$; swimming, $n = 5$; and gliding and swimming, $n = 9$) and the deep sea (crawling, $n = 3$; swimming, $n = 6$; and gliding and swimming, $n = 2$). Statistical analysis indicated no significant difference in the robot's swimming ($P = 0.84$) and crawling ($P = 0.10$) velocities between the laboratory water tank and the deep sea. Further details on the robot's multimodal locomotion in the Longxi Seamount, Haima Cold Seep, and Mariana Trench are available in movies S11 to S13.

elastic modulus that arises under higher hydrostatic pressure, to improve the locomotion amplitude and speed of the actuator in the deep sea. Additionally, the unique mechanical properties of the metamaterial structures facilitate a range of customizable and complex locomotion modes with simple actuation. This instability-induced snapping behavior and pressure-tolerant motion are inherent to bistable metamaterial structures across various configurations, scales, and materials. The ongoing development of new structures, spatial arrangements,

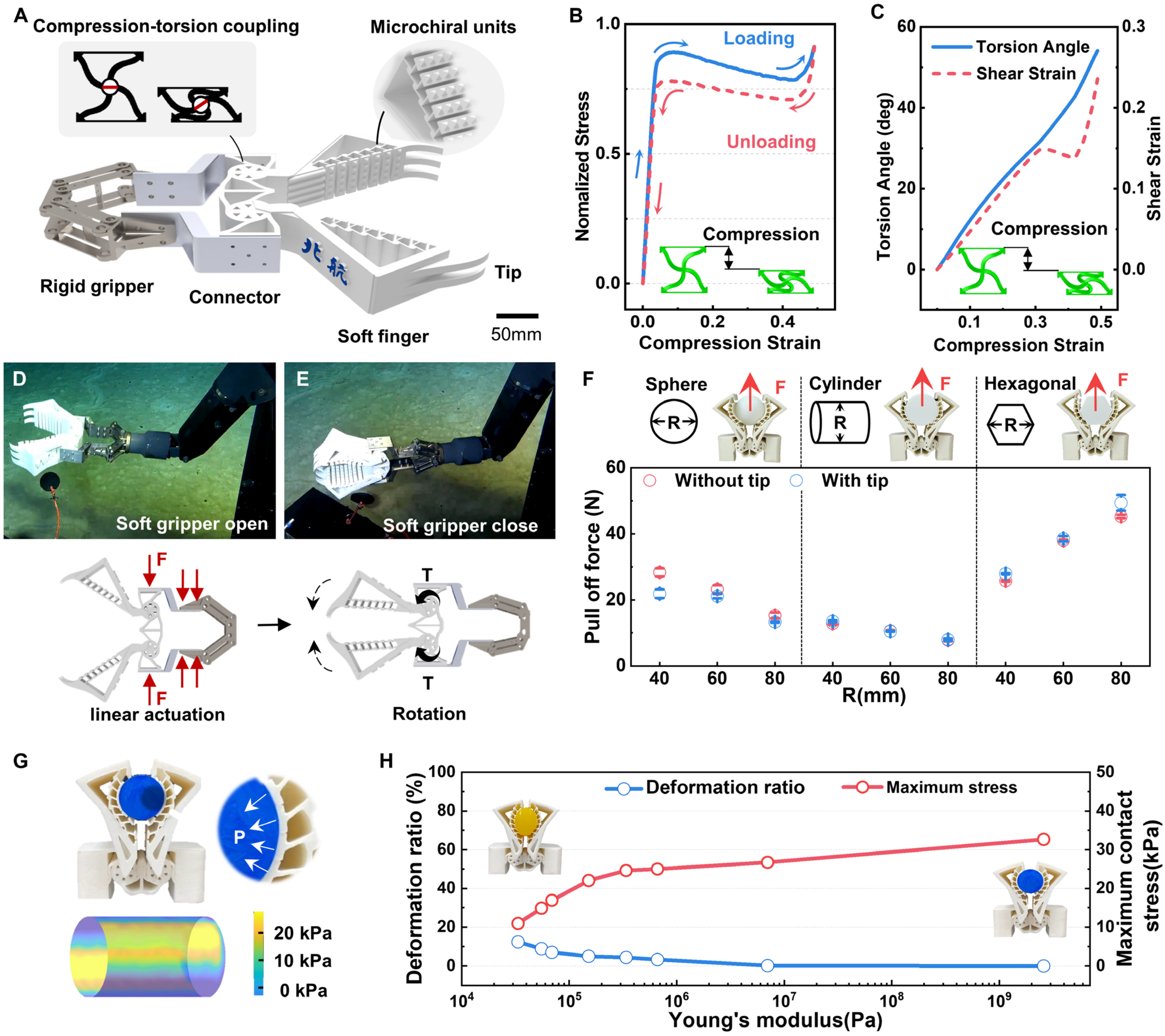

Fig. 5. Deep-sea soft gripper for delicate manipulations. (**A**) Design schematic of the gripper. The gripper consists of two symmetrical chiral units and a pair of grasping fingers. (**B**) Compression stress-strain curve of the chiral unit. (**C**) Compression-torsion and compression-shearing coupling effects of the chiral unit. (**D** and **E**) Opening and closing of the gripper's claw in the deep sea. (**F**) Maximum pull-off force of the gripper when grasping objects of various shapes and sizes ($n = 5$; error bars indicate the SD). (**G**) Contact stress exerted by the gripper while grasping a cylindrical object. (**H**) Deformation ratio and maximum contact stress of the gripper when gripping objects with different Young's moduli.

materials, and highly efficient actuators using metamaterials will further expand the design space for deep-sea soft robots capable of multimodal locomotion.

Miniaturizing deep-sea robots to a centimeter scale could offer an efficient, cost-effective robotic solution for deep-sea exploration and monitoring. By using lightweight soft actuators, our miniature robot is smaller and lighter than traditional remotely operated vehicles. The three actuation modules weigh just 48 g and require only 102 g of buoyant materials for proper balance, which makes them more than two orders of magnitude smaller than the lightest commercially available deep-sea motors, such as the S2000 series (2G Engineering, USA).

Despite its advantages, this miniature deep-sea robot has several limitations. One primary challenge is achieving perfect neutral buoyancy, given that water density in natural deep-sea environments varies with depth, location, and even time. Consequently, we designed the robot to be slightly negatively buoyant, weighing 50 g more than its equilibrium mass, on the basis of seawater density estimates from our previous submersible dives. This design ensures that the robot sinks slowly and can crawl along the seabed instead of floating upward, which would hinder effective recovery operations. Furthermore, the development of minimal buoyancy regulators at the centimeter scale to allow for buoyancy adjustments in the deep-sea robot remains an area yet to be explored.

Second, the current operational time of the robot is ~30 min. Optimizing the robot's power consumption and enhancing its energy capacity will be essential for extending deep-sea operation durations. Measuring power efficiency is particularly challenging when the flapping-based robot is self-propelled in deep-sea environments. However, the Strouhal number (*St*) serves as a useful metric to assess the efficiency of bioinspired flapping-based robots (*34*, *35*). The *St* is calculated using the formula $St = 2fh/U$, where f is the undulating frequency, h is the flapping amplitude of the caudal fin, and U is the self-propelled swimming speed. Previous studies have shown that the *St* is related to the propulsive efficiency of flapping propulsion, peaking within the optimal range of 0.2 to 0.4 (*36*). Our robot has an *St* of 0.49 during swimming in the deep sea, indicating that it is still less efficient than live fish swimming within the optimal range (*36*). To further enhance propulsion efficiency, it is important to consider factors such as the shape and size of the caudal fin, material stiffness, and flapping kinematics, which include heave, pitch, and rotational angle.

Third, the miniature robot requires improved real-time communication and autonomous control capabilities for effective deep-sea applications. Reliable communication between the robot and the crewed submersible is essential, and implementing onboard autonomous control and path planning will further enhance the robot's operational autonomy. Fourth, developing an integrated adaptive morphing structure and disturbance-resistant control strategies is essential for managing ambient flow interference, ensuring stable and efficient locomotion of the deep-sea robot.

Looking ahead, one can envision the deployment of a swarm of these miniature multimodal robots. Working collaboratively, these robots could explore the deep sea using various modalities, such as mapping the seafloor, collecting biological samples, and photographing deep-sea organisms. This collaborative approach could enhance our understanding of the deep-sea environment, opening previously unknown possibilities for exploration in this frontier.

MATERIALS AND METHODS

Design and fabrication of the deep-sea chiral actuation module

There are three main steps in fabricating the deep-sea chiral actuation module: fabricating and sealing the SMA springs, fabricating the chiral unit, and overall assembly. The fabrication and sealing of the SMA springs are crucial for the actuator's performance in high-pressure aquatic environments. Given the challenges associated with welding nitinol to conductive wires, we mechanically connected the SMA spring (0.6-mm wire diameter, 4.2-mm inner diameter) to a crimping terminal (PH2.0) using a cold pressing process (fig. S3A). Next, we inserted the SMA spring into a silicone hose (inner diameter of 1.5 mm, outer diameter of 2.5 mm) after filling the hose with silicone oil (fig. S3B). Silicone sealant was then applied to both ends of the silicone hose, which solidified completely after 4 hours (fig. S3C).

For the fabrication of the chiral unit, we first created molds for the silicone rubber cross structures using stereolithography appearance 3D printers (fig. S3D). Silicone rubber (Sil-960, Smooth-On Inc.) was poured into the molds (fig. S3E), and the cross structures were demolded after 15 hours of curing. The 3D-printed frame was then assembled into a single unit, showcasing chirality through the rotational connectors and silicone rubber cross structures (fig. S3F). In the final assembly step, the silicone tubes were attached to the ends of the rotational connectors (fig. S3G).

The chiral unit operates under torque-controlled boundary conditions, driven by the torque generated from the contracting SMA spring. As the SMA spring contracts, the applied torque increases. Once this torque reaches a critical peak value (T_{peak}), the chiral unit undergoes a snap-through process, rapidly transitioning to a second stable state, as shown in fig. S1D. Subsequently, the SMA spring on the opposite side contracts, generating an opposing torque. When the opposing torque again reaches T_{peak}, the chiral unit experiences a reverse snap-through motion, quickly returning to its original stable state. This cyclical process generates angular oscillations that mimic a fish-like flapping motion, as illustrated in fig. S1E.

The selection of the SMA is essential for achieving a sufficiently large peak torque (T_{peak}) and the corresponding driving angle (θ_{peak}) necessary to initiate the snap-through process. These parameters are intrinsically linked to the geometric characteristics of the chiral unit. Our investigation focused on two critical dimensionless parameters: the clamped ratio (λ) and the precompression strain (ε_{p}), as illustrated in fig. S2 (C and D). FEA simulations revealed a nonlinear relationship between these parameters and T_{peak} and θ_{peak}, as demonstrated in fig. S2 (E and F). To facilitate efficient switching of the bistable unit, it is crucial that T_{peak} remains within an optimal range and does not become excessively high. Consequently, we identified optimal values for the clamped ratios and precompression strains, which are indicated by star markers in fig. S2.

We optimized the selection of SMA springs, as illustrated in fig. S4, which depicts the output torque of the chiral unit across various wire diameters (d) and outer diameters (D) of the SMA springs. The findings revealed that the SMA spring with a wire diameter of 0.6 mm and an outer diameter of 4.2 mm (SMA II, fig. S4B) provides optimal performance. In contrast, the SMA spring with a smaller wire diameter (SMA I, fig. S4A) failed to produce sufficient output force (fig. S4D), because the spring with a larger wire diameter (SMA III, fig. S4C) had difficulty returning to its original position after heating and contraction. Consequently, neither SMA I nor SMA III effectively facilitated the switching process of the chiral units, making SMA II the superior choice.

Laboratory experiments of the actuator under atmospheric pressure

We conducted underwater experiments to validate the deep-sea chiral actuation module's performance. First, the chirality of the actuation module was determined by the precompressed X-shaped soft material. Therefore, we fabricated achiral modules without precompression to evaluate the contribution of chirality to the actuation performance of the module (fig. S5A and movie S3). The width of the precompressed chiral units is 38 mm, and the width of the achiral units is 45 mm. We tested the modules in a lab water tank at 5°C. Compared with achiral units, the chiral actuation module increased the swing angular velocity (with an average and maximum increase of 11.7 and 18.1 times, respectively) in the frequency range of 0.1 to 0.6 Hz (fig. S5B). We also tested the performance of the chiral actuation module under different temperatures and input frequencies (movie S4). Then, to explore the load performance of the deep-sea chiral actuation module, we conducted experimental tests in a water tank (fig. S5D). We tied weights with different masses to the end of the deep-sea chiral actuation module and actuated the module to test the maximum weights lifted by the module. The results show that the maximum output force reached 4.62 ± 1.11 N in the frequency range of 0.1 to 0.45 Hz (fig. S5E). We conducted underwater optimization experiments to determine the optimal actuation parameters for the SMA coil. At a frequency of 0.45 Hz, the optimal parameters were achieved when the heating-to-cooling time ratio was 0.3 and the actuation voltage was 9 V. Under these conditions, the rotational amplitude reached 28.18°, and the angular velocity reached 251.8°/s (fig. S5, C and F).

Pressure tank experiments of the soft actuator under high pressure

We conducted simulated deep-sea hydrostatic pressure tests in the pressure tank from the Institute of Deep-sea Science and Engineering, Chinese Academy of Sciences (fig. S5G). The deep-sea chiral actuation module, pressure-resistant camera, and light source were placed in a transparent acrylic bucket and then suspended in the pressure tank. Watertight cables connected the inside and outside of the tank, and the actuation module was driven by an external dc power supply. The loading and unloading speeds of the pressure tank were set according to the diving and surfacing speed of a crewed submersible: The loading speed was 3 MPa/min, and the unloading speed was 4 MPa/min. The maximum pressure was set to 126 MPa (fig. S5H). The actuation module was tested with a gradient of 20 MPa. The rotational amplitude and angular velocity data were obtained by tracking the actuation module connector in the video (fig. S5I).

Design and implementation of the multimodal miniature robot

The robot is capable of swimming, gliding, crawling, and morphing through its chiral actuation modules (fig. S6, A and C). When the deep-sea chiral actuation module on the right side was activated, only the right tail fin swings, generating a counterclockwise moment and forward thrust, causing the robot to turn left (fig. S6B). Conversely, activation of the left side resulted in a right turn. When both the left and right actuation modules operated simultaneously, the robot generated forward thrust and swam in a straight line.

At the initial moment of crawling (fig. S6D), the SMA on the lower side of the deep-sea chiral actuation module contracted, bringing the robot's legs together while the tail fin swings downward. At this point, the surrounding water exerted a clockwise torque on the robot around its center of mass, increasing the support and friction forces of the front foot compared with the rear foot, resulting in a forward motion. During the second instant of crawling, although the direction of the forces was reversed, the combined force continued to propel the robot forward.

The robot measures 500 mm in length, 270 mm in width, and 280 mm in height. Its weight is 1.5 kg in air and 0.05 kg in water. The shell of the robot, frame of the chiral unit, feet, and some connective elements were 3D-printed with photosensitive resin. The buoyant material comprises hollow glass microspheres and epoxy resin, with a density of 0.68 g/cm^3 and a water absorption rate of 0.6% after 24 hours under 155-MPa pressure, showing a negligible influence from pressure. The folding fins were fabricated with a silicone film bonded onto a nylon support. The horizontal connecting layer is a laser-cut acrylic plate with a customized shape. The tail fin was made of a laser-cut polyvinyl chloride plate. A printed circuit board and two batteries of 1300 mA·hour were installed in a 5 cm–by–7.4 cm–by–12.2 cm plastic box. The plastic box was connected to a silicone oil bag with changeable volume, which was filled with silicone oil to resist the high pressure of the environment. Each part of the robot was fabricated separately, making assembling and replacing parts straightforward (fig. S6E). The electronic system of the robot was mainly composed of a step-down circuit and a control circuit (fig. S6F). The voltage of the battery was regulated by a B1205 chip to generate a 5-V output from a 12.8-V input. Then, the boost step-down circuit reduced 5 to 3.3 V to power the STM32F1 chip. The STM32F1 chip provided outputs for 10 SMA springs by changing the output voltage by controlling the duty cycle.

Laboratory experiments of the robot under atmospheric pressure

We designed an experiment to explore the relationship between the propulsion force of the deep-sea chiral actuation module and the silicone modulus (fig. S7A). The deep-sea chiral actuation module is made of Pin (0 kPa), Ecoflex-0030 (68.94 kPa), Mold-star-30 (661.9 kPa), Smooth-Sil 940 (1378.95 kPa), and Smooth-Sil 960 (1930.53 kPa). We used a force sensor (ATI, min40) to record the propulsion force of the deep-sea chiral actuation module with the tail fin underwater. As the modulus increased, the propulsion force of the deep-sea chiral actuation module increased accordingly.

We characterized crawling forces on a smooth glass bottom surface and a rough sandpaper bottom surface underwater in a water tank (fig. S7, C and D). Because of the anisotropic foot design (fig. S7C), the robot's crawling forces were greater on rough surfaces than on smooth surfaces. We adjusted the robot's counterweight to make it slightly denser than water and explored its swimming, gliding, crawling, and morphing (fig. S7B) characteristics in a 1-m-deep pool. During the underwater experiments, we used a wireless transceiver module to control the robot. To explore the effect of the swinging frequency of the tail fins on the gliding and swimming speed, we conducted a set of seven gliding experiments from 0.15 to 0.45 Hz. The gliding and swimming speed increased as the frequency increased, and the maximum speed was about 6 cm/s (fig. S7F).

We tested the robot's ability to crawl in the sand and studied the influence of the robot's movement frequency and different foot sizes on the crawling speed. The same test was conducted from 0.15 to 0.45 Hz, which showed that the crawling speed increased with frequency (fig. S7I). The two foot sizes were 4 cm by 5 cm and 3 cm by 4 cm. The results show that large feet can generate higher crawling speeds than small ones. The robot could crawl straight and turn in the crawling mode (fig. S7H).

Preparations for deep-sea dives of the miniature robot

Here, we set the robot's target buoyancy to be slightly heavier than seawater, enabling it to perform both swimming and crawling in the deep sea. Using previous diving data, we obtained information about seawater density at the dive site, allowing us to adjust the robot's balance on the mother ship to ensure that it was 50 g heavier than its equilibrium mass. Before diving, the robot was preprogrammed with a delayed start, which allowed it to perform motion demonstrations after it reached the deep sea. We powered on and sealed the robot 2 hours before launching the submersible.

Statistical analysis

The experimental data collection methods used in this study were as follows: For the kinematic analysis experiments, data were collected at least three times, with each trial involving five motion cycles. Data were obtained by tracking markers with a fixed camera, with each cycle containing a minimum of 100 data points. The force experiments were repeated at least three times as well, using a force sensor with a sampling frequency of 100 Hz. To minimize dynamic interference, the movement speed of the object during these experiments was set to 3 mm/s. For the results analysis, the averages of the valid data points were used in the figures, and the SD was represented as the error bars in the figures. For field results of the robot in deep sea, we conducted multiple deep-sea dives (three times) and deployment (10 times in total) to eliminate the influence of random disturbance of ocean currents from a single deployment. All of the data are provided in the inset panel of Fig. 4F.

Supplementary Materials

The PDF file includes:

Materials and Methods
Figs. S1 to S10
Tables S1 and S2
Legends for movies S1 to S14

Other Supplementary Material for this manuscript includes the following:

Movies S1 to S14

REFERENCES AND NOTES

1. D. F. Gruber, R. J. Wood, Advances and future outlooks in soft robotics for minimally invasive marine biology. *Sci. Robot.* **7**, eabm6807 (2022).
2. B. V. Dickson, S. E. Pierce, How (and why) fins turn into limbs: Insights from anglerfish. *Earth Environ. Sci. Trans. R. Soc. Edinb.* **109**, 87–103 (2018).
3. W. Faxon, The stalk-eyed Crustacea: Reports on an exploration off the west coasts of Mexico, Central and South America, and off the Galapagos Islands, in charge of Alexander Agassiz, by the US Fish Commission Steamer "Albatross," during 1891, Lt. Commander ZL Tanner, USN, commanding. *Mem. Mus. Comp. Zool. Harv. Coll.* **18**, 1–292 (1895).
4. Y. Zhao, C. Zhang, X. Yang, X. Cao, T. Feng, F. Zhou, X. Wang, P. Zhao, T. Li, Test for the deep: Magnetic loading characterization of elastomers under extreme hydrostatic pressures. *Int. J. Extreme Manuf.* **6**, 055602 (2024).
5. K. C. Galloway, K. P. Becker, B. Phillips, J. Kirby, S. Licht, D. Tchernov, R. J. Wood, D. F. Gruber, Soft robotic grippers for biological sampling on deep reefs. *Soft Robot.* **3**, 23–33 (2016).
6. B. T. Phillips, K. P. Becker, S. Kurumaya, K. C. Galloway, G. Whittredge, D. M. Vogt, C. B. Teeple, M. H. Rosen, V. A. Pieribone, D. F. Gruber, R. J. Wood, A dexterous, glove-based teleoperable low-power soft robotic arm for delicate deep-sea biological exploration. *Sci. Rep.* **8**, 14779 (2018).
7. D. M. Vogt, K. P. Becker, B. T. Phillips, M. A. Graule, R. D. Rotjan, T. M. Shank, E. E. Cordes, R. J. Wood, D. F. Gruber, Shipboard design and fabrication of custom 3D-printed soft robotic manipulators for the investigation of delicate deep-sea organisms. *PLOS ONE* **13**, e0200386 (2018).
8. Z. E. Teoh, B. T. Phillips, K. P. Becker, G. Whittredge, J. C. Weaver, C. Hoberman, D. F. Gruber, R. J. Wood, Rotary-actuated folding polyhedrons for midwater investigation of delicate marine organisms. *Sci. Robot.* **3**, eaat5276 (2018).
9. N. R. Sinatra, C. B. Teeple, D. M. Vogt, K. K. Parker, D. F. Gruber, R. J. Wood, Ultragentle manipulation of delicate structures using a soft robotic gripper. *Sci. Robot.* **4**, eaax5425 (2019).
10. O. Khatib, X. Yeh, G. Brantner, B. Soe, B. Kim, S. Ganguly, H. Stuart, S. Wang, M. Cutkosky, A. Edsinger, P. Mullins, M. Barham, C. R. Voolstra, K. N. Salama, M. L'Hour, V. Creuze, Ocean one: A robotic avatar for oceanic discovery. *IEEE Robot. Autom. Mag.* **23**, 20–29 (2016).
11. S. Licht, E. Collins, M. L. Mendes, C. Baxter, Stronger at depth: Jamming grippers as deep sea sampling tools. *Soft Robot.* **4**, 305–316 (2017).
12. G. Li, X. Chen, F. Zhou, Y. Liang, Y. Xiao, X. Cao, Z. Zhang, M. Zhang, B. Wu, S. Yin, Y. Xu, H. Fan, Z. Chen, W. Song, W. Yang, B. Pan, J. Hou, W. Zou, S. He, X. Yang, G. Mao, Z. Jia, H. Zhou, T. Li, S. Qu, Z. Xu, Z. Huang, Y. Luo, T. Xie, J. Gu, S. Zhu, W. Yang, Self-powered soft robot in the Mariana Trench. *Nature* **591**, 66–71 (2021).
13. W. D. Shin, J. Park, H. W. Park, Bio-inspired design of a gliding-walking multi-modal robot, in *2018 IEEE/RSJ International Conference on Intelligent Robots and Systems (IROS)* (IEEE, 2018) pp. 8158–8164.
14. G. Picardi, M. Chellapurath, S. Iacoponi, S. Stefanni, C. Laschi, M. Calisti, Bioinspired underwater legged robot for seabed exploration with low environmental disturbance. *Sci. Robot.* **5**, eaaz1012 (2020).
15. T. Frenzel, M. Kadic, M. Wegener, Three-dimensional mechanical metamaterials with a twist. *Science* **358**, 1072–1074 (2017).
16. A. Rafsanjani, K. Bertoldi, A. R. Studart, Programming soft robots with flexible mechanical metamaterials. *Sci. Robot.* **4**, eaav7874 (2019).
17. L. Wen, F. Pan, X. Ding, Tensegrity metamaterials for soft robotics. *Sci. Robot.* **5**, eabd9158 (2020).
18. D. Hwang, E. J. Barron III, A. T. Haque, M. D. Bartlett, Shape morphing mechanical metamaterials through reversible plasticity. *Sci. Robot.* **7**, eabg2171 (2022).
19. W. Hu, G. Z. Lum, M. Mastrangeli, M. Sitti, Small-scale soft-bodied robot with multimodal locomotion. *Nature* **554**, 81–85 (2018).
20. Z. Ren, R. Zhang, R. H. Soon, Z. Liu, W. Hu, P. R. Onck, M. Sitti, Soft-bodied adaptive multimodal locomotion strategies in fluid-filled confined spaces. *Sci. Adv.* **7**, eabh2022 (2021).
21. D. S. Shah, J. P. Powers, L. G. Tilton, S. Kriegman, J. Bongard, R. Kramer-Bottiglio, A soft robot that adapts to environments through shape change. *Nat. Mach. Intell.* **3**, 51–59 (2021).
22. X. Liang, M. Xu, L. Xu, P. Liu, X. Ren, Z. Kong, J. Yang, S. Zhang, The AmphiHex: A novel amphibious robot with transformable leg-flipper composite propulsion mechanism, in *2012 IEEE/RSJ International Conference on Intelligent Robots and Systems* (IEEE, 2012), pp. 3667–3672.
23. A. J. Ijspeert, A. Crespi, D. Ryczko, J.-M. Cabelguen, From swimming to walking with a salamander robot driven by a spinal cord model. *Science* **315**, 1416–1420 (2007).
24. E. Hawkes, B. An, N. M. Benbernou, H. Tanaka, S. Kim, E. D. Demaine, D. Rus, R. J. Wood, Programmable matter by folding. *Proc. Natl. Acad. Sci. U.S.A.* **107**, 12441–12445 (2010).
25. Z. Zhakypov, K. Mori, K. Hosoda, J. Paik, Designing minimal and scalable insect-inspired multi-locomotion millirobots. *Nature* **571**, 381–386 (2019).
26. K. Bertoldi, V. Vitelli, J. Christensen, M. Van Hecke, Flexible mechanical metamaterials. *Nat. Rev. Mater.* **2**, 17066 (2017).
27. A. J. D. Shaikeea, H. Cui, M. O'Masta, X. R. Zheng, V. S. Deshpande, The toughness of mechanical metamaterials. *Nat. Mater.* **21**, 297–304 (2022).
28. M. S. Paterson, Effect of pressure on Young's modulus and the glass transition in rubbers. *J. Appl. Phys.* **35**, 176–179 (1964).
29. X. Zhou, W. Chen, K. Li, H. Zheng, B. Liu, S. Chen, L. Zhang, N. Qi, A 7 cm-scale spherical underwater robot using piezoelectric double-jet actuator for deep-sea environment. *IEEE/ASME Trans. Mechatron.* **29**, 3277–3288 (2024).
30. B. Zhang, D. Ji, S. Liu, X. Zhu, W. Xu, Autonomous underwater vehicle navigation: A review. *Ocean Eng.* **273**, 113861 (2023).
31. D. Prall, R. Lakes, Properties of a chiral honeycomb with a Poisson's ratio of—1. *Int. J. Mech. Sci.* **39**, 305–314 (1997).
32. X. Liu, G. Huang, G. Hu, Chiral effect in plane isotropic micropolar elasticity and its application to chiral lattices. *J. Mech. Phys. Solids* **60**, 1907–1921 (2012).
33. M. Gomez, D. E. Moulton, D. Vella, Critical slowing down in purely elastic 'snap-through' instabilities. *Nat. Phys.* **13**, 142–145 (2017).
34. G. K. Taylor, R. L. Nudds, A. L. R. Thomas, Flying and swimming animals cruise at a Strouhal number tuned for high power efficiency. *Nature* **425**, 707–711 (2003).
35. L. Wen, T. Wang, G. Wu, J. Liang, Quantitative thrust efficiency of a self-propulsive robotic fish: Experimental method and hydrodynamic investigation. *IEEE/ASME Trans. Mechatron.* **18**, 1027–1038 (2013).
36. M. S. Triantafyllou, G. S. Triantafyllou, D. K. P. Yue, Hydrodynamics of fishlike swimming. *Annu. Rev. Fluid Mech.* **32**, 33–53 (2000).

Acknowledgments: This work was supported by the National Science Foundation support projects, China (grant nos. 62425303, 92048302, T2121003, 12002016, 623B2012, and T2125009), and the National Key R&D Program of China (grant nos. 2022YFB4701800 and 2024YFB4707300). **Author contributions:** F.P., J.L., Z.Z., and L.W. conceptualized this work. F.P., J.L., Z.Z., X.H., Z.S., and J.C. developed the miniature deep-sea robot. F.P., J.L., and Z.S. developed the deep-sea soft gripper. F.P., J.L., Z.Z., X.H., Z.S., J.C., F.Y., B.C., and K.Z. performed experiments. F.P., J.L., Z.Z., X.H., H.W., Q.Z, B.C., T.J., L.H., and Y.W. visualized data. F.P., J.L., Z.Z., X.H., and L.W. wrote the manuscript. All of the authors discussed the results and commented on the manuscript. X.D., T.L., and L.W. supervised this study. **Competing interests:** The authors declare that they have no competing interests. **Data and materials availability:** The data for this study have been deposited in the database located at doi: 10.5061/dryad.dncjsxm9g.

Submitted 11 April 2024
Accepted 19 February 2025
Published 19 March 2025
10.1126/scirobotics.adp7821

Science Robotics

Miniature deep-sea morphable robot with multimodal locomotion

Fei Pan, Jiaqi Liu, Zonghao Zuo, Xia He, Zhuyin Shao, Junyu Chen, Haoxuan Wang, Qiyi Zhang, Feiyang Yuan, Bohan Chen, Tongtong Jin, Liwen He, Yun Wang, Kangle Zhang, Xilun Ding, Tiefeng Li, and Li Wen

Sci. Robot. **10** (100), eadp7821. DOI: 10.1126/scirobotics.adp7821

Science Robotics (ISSN 2470-9476) is published by the American Association for the Advancement of Science. 1200 New York Avenue NW, Washington, DC 20005. The title *Science Robotics* is a registered trademark of AAAS.